PHYSICAL REVIEW B **95**, 075126 (2017)

Spin-phonon coupling in epitaxial $Sr_{0.6}Ba_{0.4}MnO_3$ thin films

V. Goian,[1] E. Langenberg,[2,3,*] N. Marcano,[2,4] V. Bovtun,[1] L. Maurel,[3,5] M. Kempa,[1] T. Prokscha,[6] J. Kroupa,[1] P. A. Algarabel,[2,3] J. A. Pardo,[5,7,8] and S. Kamba[1]

[1]*Institute of Physics, Czech Academy of Sciences, Prague, Czech Republic*
[2]*Instituto de Ciencia de Materiales de Aragón (ICMA), Universidad de Zaragoza-CSIC, 50009 Zaragoza, Spain*
[3]*Departamento de Física de la Materia Condensada, Universidad de Zaragoza, 50009 Zaragoza, Spain*
[4]*Centro Universitario de la Defensa, Academia General Militar, 50090 Zaragoza, Spain*
[5]*Instituto de Nanociencia de Aragón (INA), Universidad de Zaragoza, 50018 Zaragoza, Spain*
[6]*Laboratory for Muon Spin Spectroscopy, Paul Scherrer Institut, CH-5232 Villigen PSI, Switzerland*
[7]*Laboratorio de Microscopías Avanzadas, Universidad de Zaragoza, 50018 Zaragoza, Spain*
[8]*Departamento de Ciencia y Tecnología de Materiales y Fluidos, Universidad de Zaragoza, 50018 Zaragoza, Spain*

(Received 22 August 2016; revised manuscript received 23 December 2016; published 15 February 2017)

Spin-phonon coupling is investigated in epitaxially strained $Sr_{1-x}Ba_xMnO_3$ thin films with perovskite structure by means of microwave (MW) and infrared (IR) spectroscopy. In this work we focus on the $Sr_{0.6}Ba_{0.4}MnO_3$ composition grown on $(LaAlO_3)_{0.3}(Sr_2AlTaO_6)_{0.7}$ substrate. The MW complex electromagnetic response shows a decrease in the real part and a clear anomaly in the imaginary part around 150 K. Moreover, it coincides with a 17% hardening of the lowest-frequency polar phonon seen in IR reflectance spectra. In order to further elucidate this phenomenon, low-energy muon-spin spectroscopy was carried out, signaling the emergence of antiferromagnetic order with Néel temperature (T_N) around 150 K. Thus, our results confirm that epitaxial $Sr_{0.6}Ba_{0.4}MnO_3$ thin films display strong spin-phonon coupling below T_N, which may stimulate further research on tuning the magnetoelectric coupling by controlling the epitaxial strain and chemical pressure in the $Sr_{1-x}Ba_xMnO_3$ system.

DOI: 10.1103/PhysRevB.95.075126

I. INTRODUCTION

Multiferroics, i.e., materials which possess two or more ferroic orders, prove worthwhile because of potential advanced applications in electric-field controlled magnetic memories, spintronics, and magnonics, especially when magnetic and ferroelectric orders are strongly coupled. Unfortunately, many multiferroics stabilize ferroic orders only at low temperatures and/or display very weak magnetoelectric coupling [1]. This fact has greatly stirred the search for unconventional mechanisms in order to create strong magnetoelectric multiferroics. One of these mechanisms is the link between the spin and the lattice degrees of freedom, known as spin-phonon coupling, which underlies strain-induced multiferroicity [2]. In recent years, first-principles calculations have predicted large spin-phonon coupling in various oxides with the perovskite structure [3,4], so these materials are good candidates to become new multiferroics under epitaxial strain or with appropriate doping.

An archetypal example of this behavior is $SrMnO_3$. Bulk $SrMnO_3$ can be stabilized at room temperature in the cubic perovskite $Pm\bar{3}m$ crystal structure, which is a paraelectric insulator with G-type antiferromagnetic (AF) order below 233 K [5]. Close to this temperature, 23% hardening of the lowest-frequency phonon was revealed in the IR spectra, proving strong spin-phonon coupling [6]. By expanding the lattice through Ba doping, ferroelectricity was successfully induced in $Sr_{1-x}Ba_xMnO_3$ ($x \geqslant 0.45$) crystals, showing ferroelectric Curie temperature $T_C \approx 400$ K and Néel temperature $T_N \approx 200$ K [7]. An important fact is that the strong ferroelectric order (characterized by high T_C and large polarization values $\approx 13\,\mu C/cm^2$) was driven by the displacement of magnetic Mn^{4+} cations, so exceptionally strong magnetoelectric coupling is expected. Terahertz spectra of $Sr_{1-x}Ba_xMnO_3$ ($x = 0.43$ and 0.45) ceramics were measured recently, showing that the AF phase transition has a huge influence on the phonon frequencies [8].

The artificial expansion of the unit cell can be accomplished also through epitaxial strain. In this regard, $SrMnO_3$ thin films deposited with 1.7% tensile strain onto (001)-oriented $(LaAlO_3)_{0.3}(Sr_2AlTaO_6)_{0.7}$ (LSAT) substrates become polar below 400 K [9]. Moreover, the polar character is severely affected by the onset of AF order at $T_N \approx 180$ K, below which a dramatic reduction of the noncentrosymmetric distortion occurs [9]. This behavior clearly resembles the temperature dependence of the tetragonal distortion in bulk $Sr_{1-x}Ba_xMnO_3$, where the magnetic superexchange interaction strongly reduces the tetragonality (defined as $|c/a-1|$, where c and a are the lattice parameters of the tetragonal structure) below T_N due to Mn^{4+} partially recovering its centrosymmetric position [7,10].

Here we aim to gain a deeper insight into the spin-phonon coupling by means of MW and IR spectroscopy in $Sr_{1-x}Ba_xMnO_3$ epitaxial thin films in which both Ba content and epitaxial strain cooperate to enlarge the crystal lattice. $Sr_{1-x}Ba_xMnO_3$ films were stabilized in the pseudocubic perovskite phase over the hexagonal ground state through epitaxial growth of coherent films on different lattice-parameter substrates [11]. In this work we will focus on epitaxially strained $Sr_{0.6}Ba_{0.4}MnO_3$ (SB40MO) thin films deposited on (001)-oriented LSAT substrates, which yield a slight tetragonal distortion [11], contrasting with the perfectly cubic structure of bulk specimens [7]. Importantly enough, we will demonstrate that SB40MO/LSAT films show strong spin-phonon coupling near T_N, proving the magnetoelectric coupling effect in perovskite $Sr_{1-x}Ba_xMnO_3$ epitaxial thin films.

*Corresponding author: eric.langenberg.perez@gmail.com

II. EXPERIMENTAL DETAILS

Epitaxial SB40MO thin films were grown on (001)-oriented LSAT substrates by pulsed laser deposition. The structural characterization of the films was carried out by x-ray diffraction (XRD) with a Bruker D8 Advance high-resolution diffractometer. The sample growth, perovskite phase stability, and structure of $Sr_{1-x}Ba_xMnO_3$ films were reported elsewhere [11].

Near-normal-incidence IR reflectivity spectra were measured using a Bruker IFS 113v Fourier-transform IR spectrometer. An Oxford Instruments Optistat optical cryostat was used for measurements between 10 and 300 K. A three-position sample holder allowed us to measure the spectra of the reference substrate and the thin film/substrate at exactly the same temperatures. The frequency range of the low-temperature IR measurements was limited by the transparency of the used polyethylene windows (up to 650 cm^{-1}), whereas the measurements at room temperature were performed up to 3000 cm^{-1}. At room temperature, two deuterated triglycine sulfate pyroelectric detectors for far- and middle-IR frequency range were used. At low temperatures, a liquid-He-cooled Si bolometer operating at 1.6 K served as far-IR detector. The reflectance spectra of the thin films and their substrates were evaluated as a two-layer optical system [12]. The reflectivity of the bulk substrate is related to complex relative permittivity $\varepsilon^*(\omega)$ and given by

$$R(\omega) = \left| \frac{\sqrt{\varepsilon^*(\omega)} - 1}{\sqrt{\varepsilon^*(\omega)} + 1} \right|^2. \quad (1)$$

It must be noted that we use different terms for mirror IR reflection from a homogeneous opaque substrate (reflectivity) and from a two-layer optical system—substrate+thin film—(reflectance). These definitions are often used in spectroscopic textbooks [13].

The bare substrate reflectivity was measured as a function of temperature and carefully fitted using the generalized factorized damped harmonic oscillator model [13]:

$$\varepsilon^*(\omega) = \varepsilon_\infty \prod_{j=1}^{n} \frac{\omega_{\mathrm{LOj}}^2 - \omega^2 + i\omega\gamma_{\mathrm{LOj}}}{\omega_{\mathrm{TOj}}^2 - \omega^2 + i\omega\gamma_{\mathrm{TOj}}}, \quad (2)$$

where ω_{TOj} and ω_{LOj} are the frequencies of the jth transverse-optical (TO) and longitudinal-optical (LO) phonons, γ_{TOj} and γ_{LOj} are the corresponding damping constants, and ε_∞ denotes the high-frequency (electronic) contribution to the permittivity determined from the room-temperature frequency-independent reflectivity above the phonon frequencies.

For the reflectance of the substrate together with the film, we kept the fitted bare substrate parameters fixed at each temperature and adjusted only the dielectric function of the film. For this purpose, we used a classical three-parameter damped oscillator model [13]:

$$\varepsilon^*(\omega) = \varepsilon_\infty + \sum_{j=1}^{n} \frac{\Delta\varepsilon_j \omega_{\mathrm{TOj}}^2}{\omega_{\mathrm{TOj}}^2 - \omega^2 + i\omega\gamma_{\mathrm{TOj}}}, \quad (3)$$

where $\Delta\varepsilon_j$ is the dielectric strength of the jth phonon. The use of the three-parameter oscillator model for the thin films is justified by the fact that the LO phonon frequencies of the films do not significantly affect the IR reflectance spectra. More details about evaluation of the two-layer optical system (substrate and semitransparent thin film) can be found elsewhere [12,14].

For MW characterization of the films, an electrodeless thin dielectric resonator method was used [15]. The $TE_{01\delta}$ resonance modes were excited in the substrates with and without film in the shielding cavity. A comparison of the resonance frequencies and quality factors of the resonators with and without film allows calculation of the in-plane averaged dielectric parameters in the film at the resonance frequency. Precisely the same thickness of bare substrate and substrate with film is needed for the accurate evaluation of the film parameters. The measurements were performed using an Agilent E8364B vector network analyzer and a Janis closed-cycle He cryostat (10–400 K). In the case of SB40MO film, 480-μm-thick (001) LSAT square substrates (10 mm × 10 mm) were used at the resonance frequency ≈13.1 GHz.

Let us note that resonance frequencies and quality factors of the $TE_{01\delta}$ dielectric resonators are generally defined by both complex relative dielectric permittivity ε^* and relative magnetic permeability μ^* of the material. In the following we will use the standard notation ε' and μ' to denote the real part and ε'' and μ'' to denote the imaginary part of the relative dielectric permittivity and magnetic permeability, respectively. In the case of nonmagnetic materials, $\mu^* = 1 + i0$ and dielectric parameters of the film are determined using the thin dielectric resonator method. But in our case of multiferroic materials, both ε^* and μ^* should be taken into account. Consequently, we cannot separate magnetic and dielectric contributions and we are able to obtain only the real and imaginary parts of the product $\varepsilon^*\mu^*$, which we will call the complex electromagnetic response.

If we take into account the very small thickness of the films (13 nm) with respect to that of the substrates (480 μm) and an uncertainty of the substrate thickness at the micrometer level together with a limited precision of the thin film parameters calculation procedure [15], one can understand that absolute values of the MW $\varepsilon^*\mu^*$ film parameters are only a rough estimation. Nevertheless, the thin dielectric resonator method provides very high sensitivity to the relative changes of the $\varepsilon^*\mu^*$ film parameters with temperature [15]. Therefore we consider temperature changes of the real $\mathrm{Re}(\varepsilon^*\mu^*)$ and imaginary $\mathrm{Im}(\varepsilon^*\mu^*)$ parts of the film complex electromagnetic response as reliable characteristics and use them for indication of possible phase transitions of both magnetic and ferroelectric nature.

Muon-spin relaxation and rotation (μSR) measurements were carried out using the low-energy muon spectrometer at the μE4 beamline of the Paul Scherrer Institut (PSI, Switzerland) [16]. In μSR experiments spin-polarized positive muons are implanted into a sample and thermalized. Each implanted muon decays with a lifetime $\tau_\mu = 2.2\ \mu$s emitting a positron preferentially in the direction of its spin at the time of the decay. Thus, by detecting the muons at their implantation time and the positrons after the decay, the temporal evolution of the muon-spin polarization (proportional to the decay asymmetry) in a sample can be measured to obtain information about the local environment of the muons.

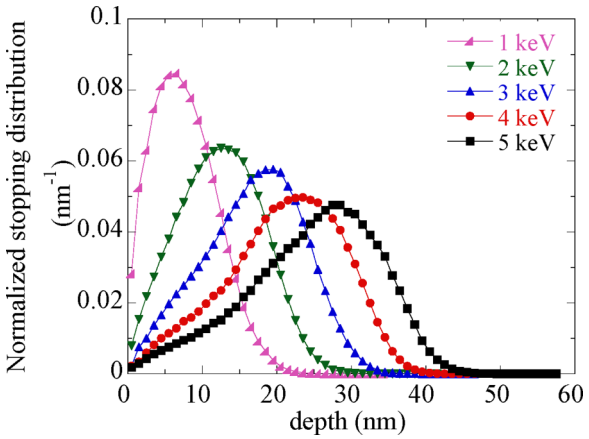

FIG. 1. The normalized stopping distribution of muons with different implantation energies in a $Sr_{0.6}Ba_{0.4}MO_3$ film deposited on a single-crystal LSAT substrate, calculated using TRIM.SP. The lines are a guide for the eye.

In μSR experiments with bulk materials, muons with energy 4.1 MeV are used. In this case, the mean stopping depth in condensed matter is $\approx$100 μm. To investigate thin films low-energy muon spin spectroscopy (LE-μSR) uses epithermal muons ($\approx$15 eV), which are created by moderating surface muons. After reacceleration, the final energy of the muons is adjusted by using a bias voltage applied at the sample. By tuning the implantation energy between 1 and 30 keV, mean depths between 10 nm and a few hundred nanometers can be chosen. More details on μSR techniques, in general, and LE-μSR, in particular, can be found in Refs. [17–19].

To determine where the muons would implant within the sample we carried out Monte Carlo simulations using the TRIM.SP software [20]. The results of these calculations in our samples for different implantation energies are shown in Fig. 1. By tuning the energy between 1 and 5 keV the mean stopping depth of the muons can be varied in a range of 5–30 nm in this film. The data presented here were obtained with a muon implantation energy $E_{\mathrm{imp}} = 1$ keV. This energy yields a mean implantation depth of about 5 nm and approximately 87% of the muons stopped at the SB40MO film.

The experiments were performed in ultrahigh vacuum at a pressure of 10^{-9} mbar in the temperature range 5–300 K. LE-μSR measurements were carried out in a weak transverse magnetic field of 10 mT to determine the magnetic transition temperature T_N.

For the second-harmonic generation (SHG) study we used a custom-made setup with a Q-switched Nd-YAG laser ($\lambda =$ 1064 nm, 20 Hz, $\sim$0.5 mJ/pulse, 6 ns) as the light source. The filtered second-harmonic signal at 532 nm was detected by a photomultiplier and a boxcar averager. SHG measurements were performed down to 100 K using a Linkam THMS 600 temperature cell.

III. RESULTS AND DISCUSSION

Figure 2 shows the XRD analysis—$\theta/2\theta$ diffractogram around the (002) pseudocubic reflection and reciprocal space map around the (103) pseudocubic reflection—of the 13-nm-thick SB40MO film that is to be analyzed in this work. Accordingly, the SB40MO epitaxial film is stabilized in the perovskite phase and grows fully strained on LSAT with in-plane and out-of-plane lattice parameters $a = 3.867$ Å and $c = 3.920$ Å, respectively. Thus, the structure presents a tetragonal distortion (c/a–1 = 1.4%), with an elongated out-of-plane lattice parameter due to the compressive epitaxial strain imposed by the substrate. Note that bulk SB40MO is perfectly cubic [7]. A deeper discussion regarding the structure of strained $Sr_{1-x}Ba_xMnO_3$ thin films can be found elsewhere [11].

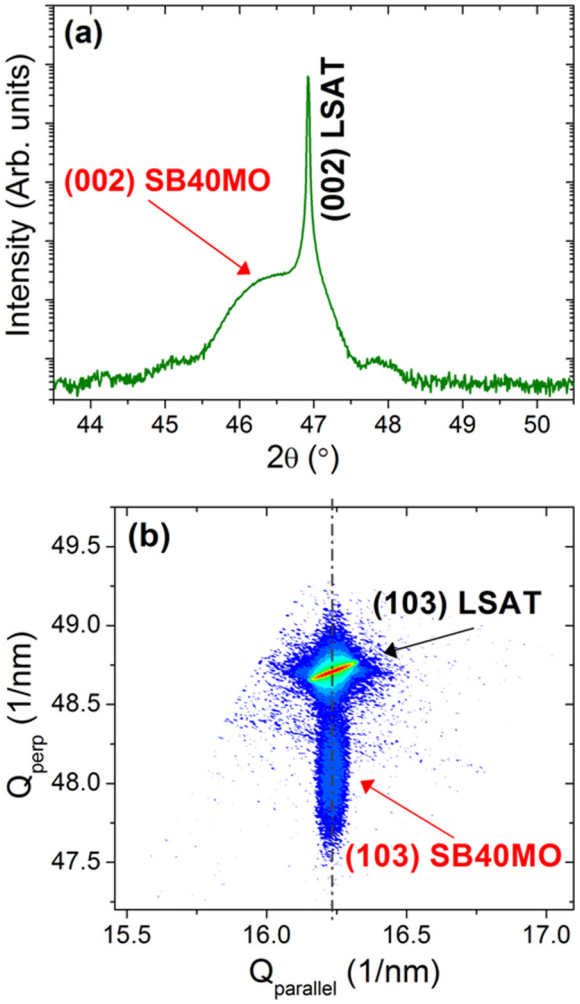

FIG. 2. XRD of SB40MO grown on (001)-oriented LSAT: (a) $\theta/2\theta$ diffractogram around the pseudocubic (002) reflection. (b) Reciprocal space map around the (103) pseudocubic reflection.

First we proceed to evaluate the IR reflectance spectra of SB40MO/LSAT (Fig. 3). As LSAT substrate is cubic, its phonon spectrum is simple and moreover phonon parameters are only slightly temperature dependent (see Fig. S1 in the Supplemental Material [21]). This makes the analysis of the phonon spectra of SB40MO/LSAT manageable. IR reflectance was measured from 300 K down to 10 K and fitted using Eq. (3) and the procedure described in Ref. [12] (see Fig. 3). From the fits we evaluated the TO phonon frequencies,

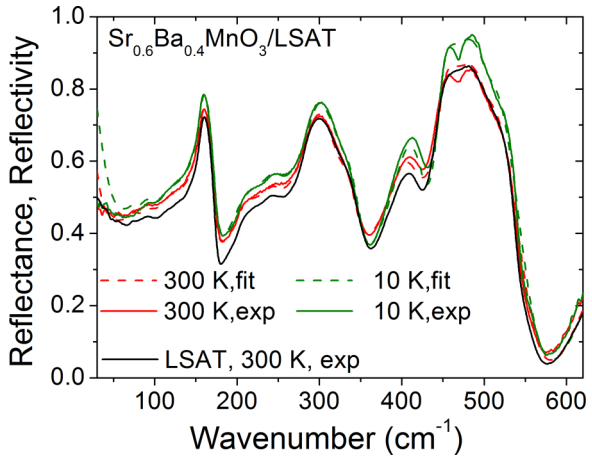

FIG. 3. Infrared reflectance spectra of SB40MO/LSAT thin film at 10 and 300 K, and reflectivity of LSAT at 300 K. Solid lines correspond to the experimentally measured spectra and dashed lines are the fits using Eq. (3).

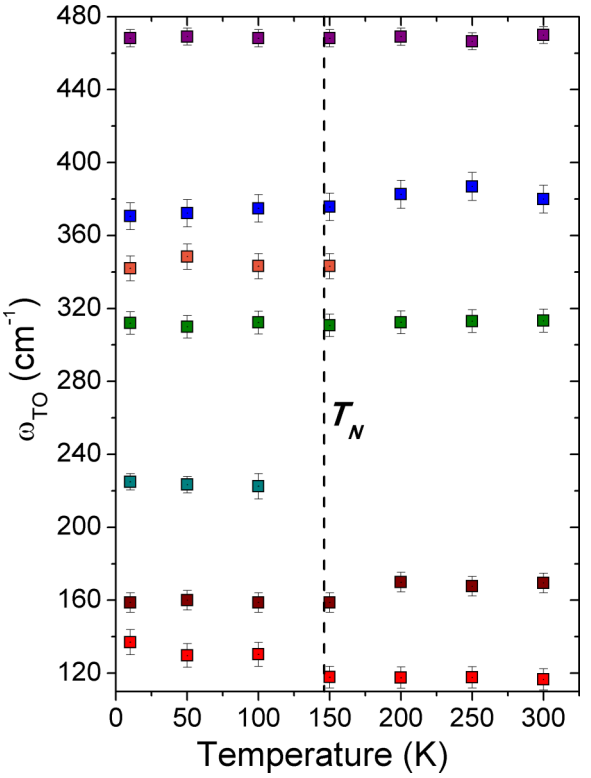

FIG. 4. Temperature dependence of transverse-optical phonon frequencies obtained from the fits of the thin film spectra. The vertical dashed line indicates the Néel temperature obtained from LE-μSR measurements [see Fig. 6(b)].

dampings, dielectric strengths, and calculated complex dielectric response $\varepsilon^*(\omega)$. One can argue that the difference between the spectra of the bare substrate and the substrate with the film is small, and therefore the accuracy of determination of phonon parameters is rather limited. Nevertheless, as shown in Fig. S2 in the Supplemental Material [21], in which two room-temperature spectra obtained at different conditions are depicted, the sensitivity and reproducibility of our spectra are very high and therefore the obtained phonon frequencies are highly ($\pm 2\%$) reliable.

Temperature dependencies of the phonon frequencies and the real parts of the $\varepsilon^*(\omega)$ spectra and the complex conductivity (ε' and σ', respectively) at selected temperatures are shown in Figs. 4 and 5. Note that σ' in $\Omega^{-1}\,\mathrm{cm}^{-1}$ is obtained from the imaginary part, ε'', of the $\varepsilon^*(\omega)$ spectra using the following expression $\sigma' = 60\varepsilon''\omega$ [14]. At room temperature, five TO phonons are resolved in the SB40MO thin film (see Fig. 4). Five similar modes were also observed in $Sr_{0.55}Ba_{0.45}MnO_3$ ceramics [8]. Two additional TO phonons are activated below 150 and 100 K, which could be a signature of some symmetry lowering phase transition, but a more plausible explanation is just their activation due to lower phonon damping at low temperatures. Although only three polar phonons are allowed in the cubic perovskite phase, seven modes can be partially explained by two cations (Sr and Ba) with different mass on the *A*-perovskite site, which would cause the observed splitting of all modes. This effect is called two-mode behavior and it is well known in many materials [22] including bulk $Sr_{0.55}Ba_{0.45}MnO_3$ ceramics [8]. Even if we take into account that our strained thin films show tetragonal structure, we can see only in-plane polarized phonons (i.e., *E* symmetry modes) and again, they can be split due to the two-mode behavior. On the other hand, we cannot exclude phonon splitting below T_N due to exchange coupling, which can locally break the crystal symmetry. This was already reported in transition-metal monoxides and in the frustrated AF oxide spinels [23], and it is probably responsible for the activation of at least one from the seven modes.

It is worth noting that the lowest-frequency phonon (TO1) significantly hardens below 150 K, i.e., from $120\,\mathrm{cm}^{-1}$ to $140\,\mathrm{cm}^{-1}$ corresponding to a 17% increase. In bulk cubic $Sr_{1-x}Ba_xMnO_3$, this mode is associated with the displacement of the Mn^{4+} cation with regard to the surrounding oxygen octahedron and is thus responsible for the polar distortions in samples with $x > 0.4$ [24]. Similar phonon frequency hardening is found below the Néel temperature in bulk specimens due to the strong spin-phonon coupling [6–8,24], in which the frequency of the TO1 phonon mode follows: $\omega_{TO1}^2 = \omega_{TO1,PM}^2 + \lambda\langle \boldsymbol{S}_i \cdot \boldsymbol{S}_j \rangle$, where $\omega_{TO1,PM}$ is the phonon frequency in the paramagnetic regime, λ is the spin-phonon coupling constant, and $\langle \boldsymbol{S}_i \cdot \boldsymbol{S}_j \rangle$ is the nearest-neighbor spin correlation function [24,25]. Being $\lambda\langle \boldsymbol{S}_i \cdot \boldsymbol{S}_j \rangle > 0$ in the AF regime [7,24], the frequency of the phonon is expected to increase when the AF order emerges. Thus, it seems reasonable to argue that SB40MO/LSAT orders antiferromagnetically below 150 K and displays sizable spin-phonon coupling, as will be discussed later on.

The peaks observed in the frequency dependence of conductivity σ' are associated to the TO phonon frequencies [see Fig. 5(b)]. Yet the lowest-frequency mode has the strongest contribution $\Delta\varepsilon_j$ to ε' [Fig. 5(a)]. The phonon contribution to the static relative dielectric permittivity $\varepsilon'(0) = \varepsilon_\infty + \sum_{j=1}^{n} \Delta\varepsilon_j$, where $\Delta\varepsilon_j$ and ε_∞ have the same meaning as in Eq. (3), presents a drop below 150 K, as depicted in Fig. 6(a), corresponding to the aforementioned hardening of the lowest-frequency mode. This reduction of the dielectric

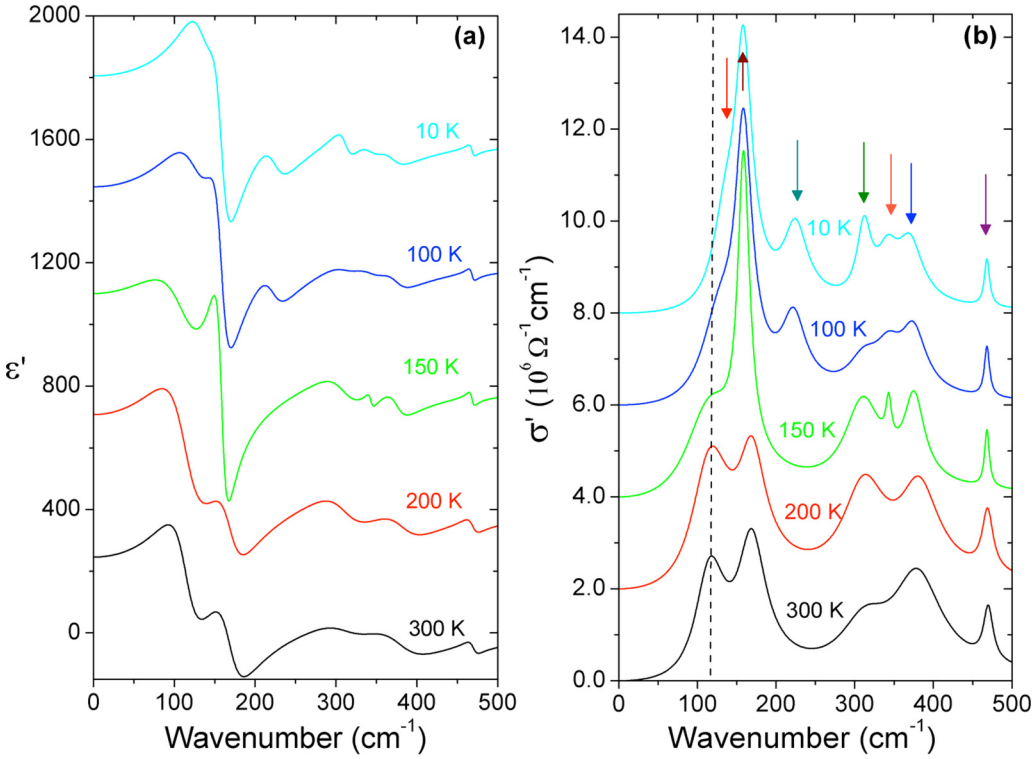

FIG. 5. Real parts of complex permittivity (a) and conductivity (b) obtained from the fits of IR reflectance spectra. Offsets of 400 and 2×10^6 were used in ε' and σ' spectra, respectively. Phonon frequencies are marked by arrows in the 10 K spectrum of σ'. The dashed line marks the frequency of the lowest-frequency phonon at 300 K (its shift towards higher wave numbers on cooling is clearly seen). Full width at half maximum of each contribution corresponds to phonon damping. Newly activated phonons appear near 220 and 340 cm^{-1} below 100 and 150 K, respectively.

constant arising from the increase of the TO1 mode frequency below T_N is also observed in archetypal spin-phonon coupling oxide $EuTiO_3$ [26,27].

In order to investigate this plausible AF transition in the thin films, associated with the hardening of the lowest-frequency mode, we performed LE-μSR measurements. The experimental study of AF ordering in thin films is challenging due to the large diamagnetic signal of the substrate in comparison to the film. LE-μSR allows stopping muons in matter at different depths in the nanometer range, and is therefore well suited to address this problem. This technique was successfully used before to determine the ordering temperature in AF thin films such as $La_{2-x}Sr_xCuO_4$ [28], $TbMnO_3$ [29], $Pr_{0.5}Ca_{0.5}MnO_3$ [30], and more recently in strained multiferroic $SrMnO_3$ [31]. The method used here to determine the Néel temperature is identical to the one described in Ref. [30].

The Néel temperature was determined from temperature scans in a weak magnetic field B_{ext} applied perpendicular to the initial muon-spin polarization and to the film surface. The decay rate of the muon-spin polarization is described by the relaxation function

$$G_x(t) = f_T^{TF} \cos(\gamma_\mu B_l t + \phi) e^{-\lambda_T t} + f_L^{TF} e^{-\lambda_L t}, \quad (4)$$

which represents the paramagnetic part of the muon-spin polarization. f_T^{TF} and f_L^{TF} reflect the fraction of the muons having their spin initially transverse and longitudinal to the local magnetic field direction, respectively. The first term describes the muon precession with frequency $\omega_\mu = \gamma_\mu B_l$ in the local magnetic field B_l at the muon stopping site, where $B_l = B_{\text{ext}}$ above and below T_N in our case. ϕ is a phase offset due to the spin rotation of the implanted muons relative to the positron detectors. The relaxation rate λ_T describes how fast this precession is depolarized by a distribution or fluctuations of magnetic fields (relaxation by static and dynamic effects). The second term represents the part of nonprecessing muon spins. Relaxation can appear here in the presence of fluctuating magnetic fields (relaxation only by dynamics). The fitting of the relaxation function $G_x(t)$ was performed using the MUSRFIT program [32].

Above T_N (in the paramagnetic regime) f_T^{TF} is at its maximum, since only B_{ext} is present inside the sample. Below T_N, the superposition of the small external B_{ext} and the internal magnetic fields in the sample leads to a strong dephasing of the precession signal. This produces a decrease of f_T^{TF} to a level corresponding to the nonmagnetic volume fraction of the sample. A decrease in f_T^{TF} with a simultaneous increase in f_L^{TF} demonstrates static magnetism (see [30] for details).

Figure 6(b) shows the transverse fraction f_T^{TF} as a function of temperature for the SB40MO film deposited on a LSAT substrate. The data are normalized to the values in the paramagnetic regime at 300 K. The magnetic transition manifests a decay of the transverse fraction $f_T^{TF}(T)/f_T^{TF}(300\,\text{K})$ at a temperature around 150 K. T_N is obtained by fitting the derivative curve of the data with a Gaussian curve and taking its center as T_N. This yields a value of $T_N = 146(4)$ K, in good

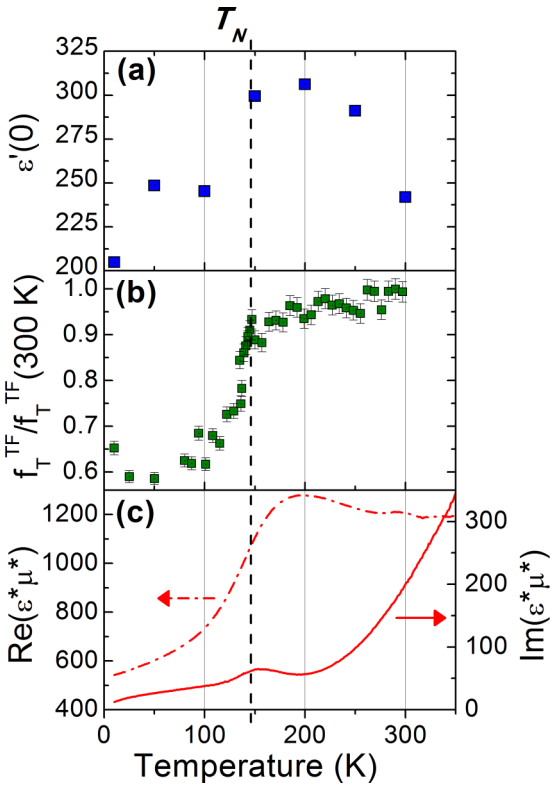

FIG. 6. (a) Static dielectric permittivity of SB40MO/LSAT film from the phonon contribution obtained by IR reflectance spectra fits. (b) Temperature dependence of the transverse fraction f_T^{TF} of the muons determined in an external transverse magnetic field of 10 mT for $E_{\text{impl}} = 1$ keV, normalized to the fraction at 300 K for SB40MO film on LSAT. (c) Temperature dependencies of the real (left axis) and imaginary (right axis) parts of microwave complex electromagnetic response $\varepsilon^*\mu^*$ of the SB40MO/LSAT thin film obtained at 13.1 GHz. The vertical dashed line indicates the Néel temperature determined from LE-μSR measurements (see text).

agreement with the temperature where hardening of the TO1 mode occurs (Fig. 4).

In order to get a deeper insight into these phenomena, the temperature dependence of the MW in-plane complex electromagnetic response $\varepsilon^*\mu^*$ of the SB40MO/LSAT film was measured at 13.1 GHz, as shown in Fig. 6(c). The real part $\text{Re}(\varepsilon^*\mu^*)$ exhibits a drop below 180 K, which also points to the effect of the onset of the AF ordering below this temperature, as μ' usually decreases below T_N. The maximum slope of $\text{Re}(\varepsilon^*\mu^*)$ closely agrees with the Néel temperature previously determined. Most important is the fact that $\varepsilon'(T)$ also decreases below 150 K as determined from the phonon contribution [Fig. 6(a)]. Hence, the observed decrease of $\text{Re}(\varepsilon^*\mu^*)$ is due to the decrease of both $\varepsilon'(T)$ and $\mu'(T)$. On the other hand, the imaginary part $\text{Im}(\varepsilon^*\mu^*)$ exhibits a peak near 150 K as shown in Fig. 6(c). It is mainly related to the maximum of magnetic losses μ'' and indicates that the AF phase transition temperature T_N is around 150 K in good agreement with LE-μSR experiments.

According to Ref. [7], bulk $Sr_{1-x}Ba_xMnO_3$ is ferroelectric for $x \geqslant 0.43$. It is known that epitaxial strain can induce ferroelectric order in paraelectric systems such as $EuTiO_3$ [2] or $SrTiO_3$ [33], so the question arises whether our compressively strained SB40MO/LSAT film can be ferroelectric. It is known that 1.7% tensile-strained $SrMnO_3$ film becomes polar [9], so one can naively expect that smaller strain can induce ferroelectric phase in SB40MO, because it has larger unit parameters than $SrMnO_3$. Unfortunately, we did not observe any ferroelectric anomaly in the temperature dependence of the microwave $\varepsilon^*\mu^*$ response [Fig. 6(c)], and furthermore polar phonons do not exhibit any softening typical for displacive ferroelectric phase transitions. However, in a compressively strained film, polarization and dielectric anomaly should arise out of film plane [32,34] and our microwave and IR studies are sensitive only to in-plane response. This means we cannot detect the ferroelectric phase transition even if it exists. Compressive strain also explains the observed higher TO1 mode frequency than in bulk $Sr_{0.57}Ba_{0.43}MnO_3$ ceramics [8]. Polar noncentrosymmetric phase can be, in principle, revealed by measurement of the SHG signal, but our preliminary SHG experiment did not reveal any signal down to the lowest achieved temperature, 100 K. Experiments to investigate tensile-strained $Sr_{1-x}Ba_xMnO_3$ thin films which are expected to exhibit ferroelectricity with lower content of Ba than in the bulk and higher strain are underway. They are predicted to become not only ferroelectric but also ferromagnetic for tensile strain values larger than 3.5% [35].

IV. CONCLUSIONS

In summary, we have demonstrated the interplay between magnetic order, phonon relations, and dielectric properties in strained $Sr_{0.6}Ba_{0.4}MnO_3$ epitaxial thin films grown on LSAT. They were proved to become antiferromagnetic below $T_N \approx 150$ K, which is lower than in bulk specimens. The onset of the antiferromagnetic order gives rise to a strong decrease in the real part of the complex electromagnetic response $\varepsilon^*\mu^*$, whereas a maximum in the imaginary part of $\varepsilon^*\mu^*$ is found around T_N. Moreover, infrared reflectance spectra reveal a remarkable (17%) hardening of the lowest-frequency phonon mode below T_N, which yields a noticeable reduction of the dielectric permittivity in the antiferromagnetic regime. Our results, hence, show that strained $Sr_{0.6}Ba_{0.4}MnO_3$ thin films display sizable spin-phonon coupling, which might be relevant to further studying magnetoelectric properties in the $(Sr,Ba)MnO_3$ system by strain engineering and chemical pressure.

ACKNOWLEDGMENTS

Part of this work was supported by the Czech Science Foundation (Projects No. 14-14122P and No. 15–08389S) and by MŠMT KONTAKT II project LH 15122. Financial support from Spanish Ministerio de Economía y Competitividad through project MAT2014-51982-C2 and from regional Gobierno de Aragón through project E26 including FEDER funding is also acknowledged. The low-energy μSR measurements have been performed at the Swiss Muon Source SμS, Paul Scherrer Institut, Villigen, Switzerland.

[1] S. Dong, J.-M. Liu, S.-W. Cheong, and R. Zhifeng, Adv. Phys. **64**, 519 (2015).

[2] J. H. Lee, L. Fang, E. Vlahos, X. Ke, Y. W. Jung, L. Fitting Kourkoutis, J.-W. Kim, P. J. Ryan, T. Heeg, M. Roeckerath, V. Goian, M. Bernhagen, R. Uecker, P. Ch. Hammel, K. M. Rabe, S. Kamba, J. Schubert, J. W. Freeland, D. A. Muller, C. J. Fennie, P. E. Schiffer, V. Gopalan, E. Johnston-Halperin, and D. G. Schlom, Nature (London) **466**, 954 (2010).

[3] J. Hong, A. Stroppa, J. Íñiguez, S. Picozzi, and D. Vanderbilt, Phys. Rev. B. **85**, 054417 (2012).

[4] J. H. Lee and K. M. Rabe, Phys. Rev. Lett. **104**, 207204 (2010).

[5] O. Chmaissem, B. Dabrowski, S. Kolesnik, J. Mais, D. E. Brown, R. Kruk, P. Prior, B. Pyles, and J. D. Jorgensen, Phys. Rev. B **64**, 134412 (2001).

[6] S. Kamba, V. Goian, V. Skoromets, J. Hejtmánek, V. Bovtun, M. Kempa, F. Borodavka, P. Vaněk, A. A. Belik, J. H. Lee, O. Pacherová, and K. M. Rabe, Phys. Rev. B **89**, 064308 (2014).

[7] H. Sakai, J. Fujioka, T. Fukuda, D. Okuyama, D. Hashizume, F. Kagawa, H. Nakao, Y. Murakami, T. Arima, A. Q. R. Baron, Y. Taguchi, and Y. Tokura, Phys. Rev. Lett. **107**, 137601 (2011).

[8] V. Goian, F. Kadlec, C. Kadlec, B. Dabrowski, S. Kolesnik, O. Chmaissem, D. Nuzhnyy, M. Kempa, V. Bovtun, M. Savinov, J. Hejtmánek, J. Prokleška, and S. Kamba, J. Phys.: Condens. Mater. **28**, 175901 (2016).

[9] C. Becher, L. Maurel, U. Aschauer, M. Lilienblum, C. Magén, D. Meier, E. Langenberg, M. Trassin, J. Blasco, I. P. Krug, P. A. Algarabel, N. A. Spaldin, J. A. Pardo, and M. Fiebig, Nat. Nanotechnol. **10**, 661 (2015).

[10] D. K. Pratt, J. W. Lynn, J. Mais, O. Chmaissem, D. E. Brown, S. Kolesnik, and B. Dabrowski, Phys. Rev. B **90**, 140401(R) (2014).

[11] E. Langenberg, R. Guzmán, L. Maurel, L. Martínez de Baños, L. Morellón, M. R. Ibarra, J. Herrero-Martín, J. Blasco, C. Magén, P. A. Algarabel, and J. A. Pardo, ACS Appl. Mater. Interfaces **7**, 23967 (2015).

[12] V. Železný, I. Fedorov, and J. Petzelt, Czech J. Phys. **48**, 537 (1988).

[13] F. Gervais, *Infrared and Millimeter Wave* (Academic, New York, 1983).

[14] B. P. Gorshunov, A. A. Volkov, A. S. Prokhorov, and I. E. Spektor, Phys. Solid State **50**, 2001 (2008).

[15] V. Bovtun, V. Pashkov, M. Kempa, S. Kamba, A. Eremenko, V. Molchanov, Y. Poplavko, Y. Yakymenko, J. H. Lee, and D. G. Schlom, J. Appl. Phys. **109**, 024106 (2011).

[16] T. Prokscha, E. Morenzoni, K. Deiters, F. Foroughi, D. George, R. Kobler, A. Suter, and V. Vrankovic, Nucl. Instrum. Methods Phys. Res., Sect. A **595**, 317 (2008).

[17] A. Yaouanc and P. Dalmas de Réotier, *Muon Spin Rotation, Relaxation, and Resonance—Applications to Condensed Matter* (Oxford University Press, Oxford, 2011).

[18] E. Morenzoni, T. Prokscha, A. Suter, H. Luetkens, and R. Khasanov, J. Phys.: Condens. Matter **16**, S4583 (2004).

[19] P. Bakule and E. Morenzoni, Contemp. Phys. **45**, 203 (2004).

[20] W. Eckstein, *Computer Simulation of Ion-Solid Interactions* (Springer, Berlin, 1991).

[21] See Supplemental Material at http://link.aps.org/supplemental/10.1103/PhysRevB.95.075126 for additional figures.

[22] A. S. J. Barker and A. J. Sievers, Rev. Mod. Phys. **47**, S1 (1975).

[23] C. Kant, M. Schmidt, Z. Wang, F. Mayr, V. Tsurkan, J. Deisenhofer, and A. Loidl, Phys. Rev. Lett. **108**, 177203 (2012).

[24] H. Sakai, J. Fujioka, T. Fukuda, M. S. Bahramy, D. Okuyama, R. Arita, T. Arima, A. Q. R. Baron, Y. Taguchi, and Y. Tokura, Phys. Rev. B. **86**, 104407 (2012).

[25] C. J. Fennie and K. M. Rabe, Phys. Rev. Lett. **97**, 267602 (2006).

[26] T. Katsufuji and H. Takagi, Phys. Rev. B **64**, 054415 (2001).

[27] S. Kamba, V. Goian, M. Orlita, D. Nuzhnyy, J. H. Lee, D. G. Schlom, K. Z. Rushchanskii, M. Ležaić, T. Birol, C. J. Fennie, P. Gemeiner, B. Dkhil, V. Bovtun, M. Kempa, J. Hlinka, and J. Petzelt, Phys. Rev. B **85**, 094435 (2012).

[28] E. Stilp, A. Suter, T. Prokscha, E. Morenzoni, H. Keller, B. M. Wojek, H. Luetkens, A. Gozar, G. Logvenov, and I. Božović, Phys. Rev. B **88**, 064419 (2013).

[29] M. Bator, Y. Hu, H. Luetkens, C. Niedermayer, T. Prokscha, A. Suter, Z. Salman, M. Kenzelmann, C. H. Schneider, and T. Lippert, Phys. Procedia **30**, 137 (2012).

[30] I. Komissarov, Y. Zhang, G. J. Nieuwenhuys, E. Morenzoni, T. Prokscha, A. Suter, and J. Aarts, Europhys. Lett. **83**, 47013 (2008).

[31] L. Maurel, N. Marcano, T. Prokscha, E. Langenberg, J. Blasco, R. Guzmán, A. Suter, C. Magen, L. Morellón, M. R. Ibarra, J. A. Pardo, and P. A. Algarabel, Phys. Rev. B **92**, 024419 (2015).

[32] A. Suter and B. M. Wojek, Phys. Procedia **30**, 69 (2012).

[33] J. H. Haeni, P. Irvin, W. Chang, R. Uecker, P. Reiche, Y. L. Li *et al.*, Nature (London) **430**, 758 (2004).

[34] O. Diéguez, K. M. Rabe, and D. Vanderbilt, Phys. Rev. B **72**, 144101 (2005).

[35] H. Chen and A. J. Millis, Phys. Rev. B **94**, 165106 (2016).